fig. S1

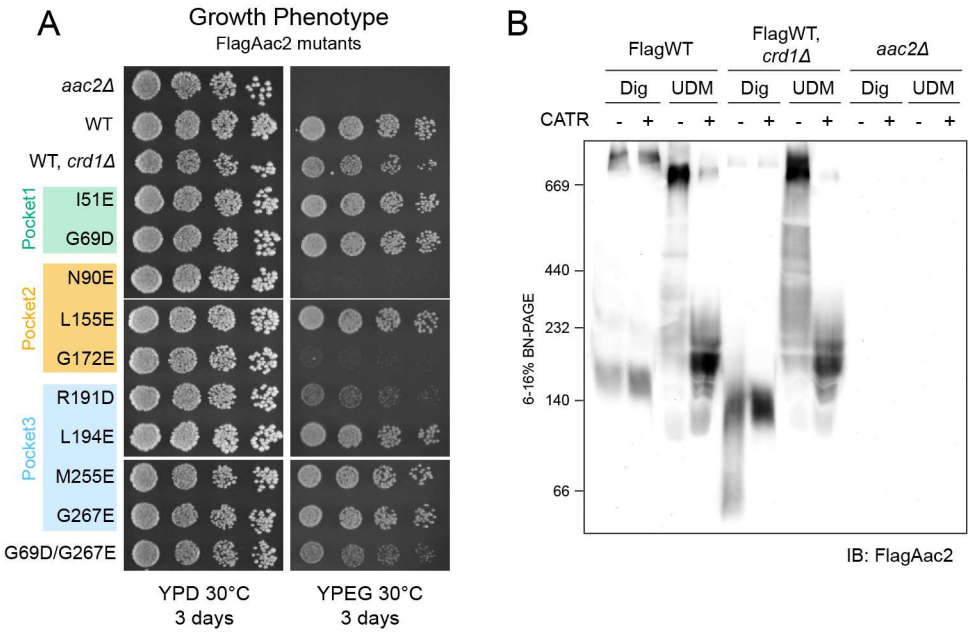

fig. S1: Characterization of Flag-tagged WT and mutant Aac2. (A) Growth phenotype of Flag-tagged Aac2 CL-binding mutants. Serial dilutions of indicated cells were spotted onto fermentable (YPD) and respiratory (YPEG) media and incubated at 30ºC for 3 days (n=3). (B) Mitochondria from indicated strains were mock- or pre-treated with 40 µM CATR. The treated mitochondria were then solubilized with 1.5% (w/v) digitonin or 2% (w/v) UDM, resolved by 6 to 16% blue native-PAGE and immunoblotted for Flag. Representative image from the replicates (n=3) is shown.

fig. S2

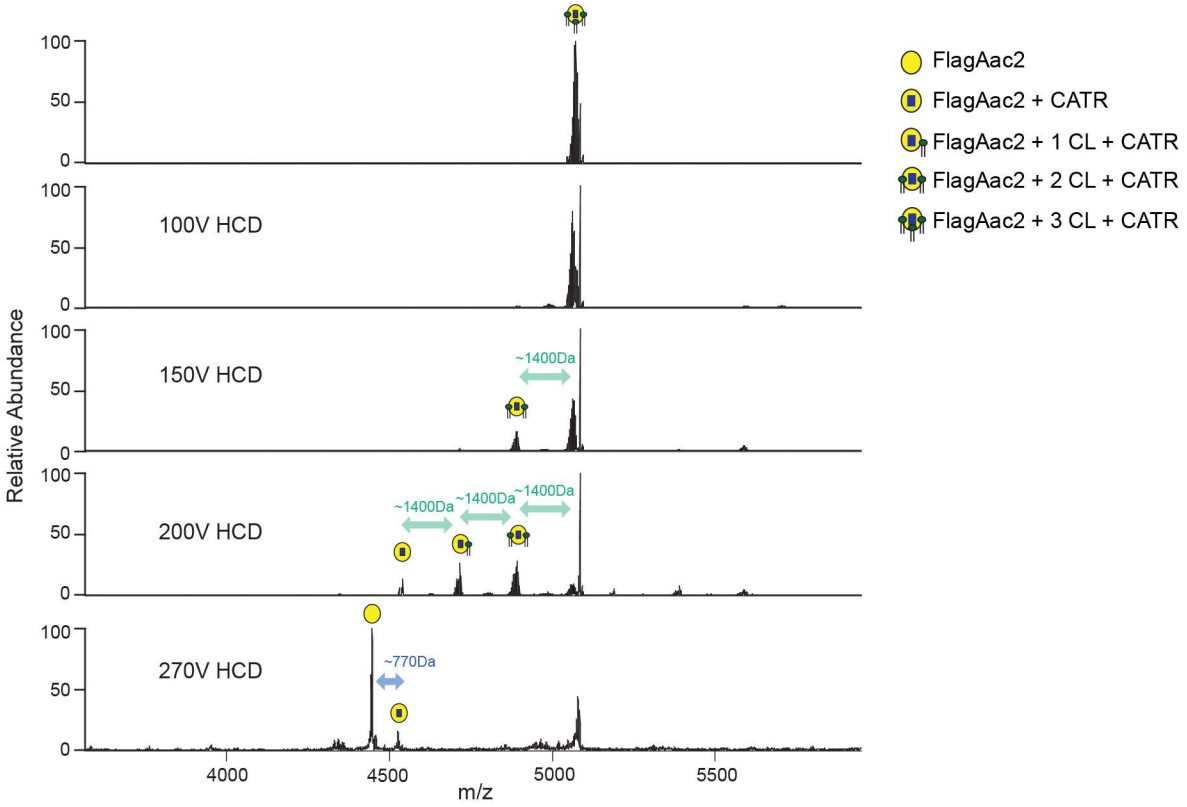

fig. S2: Three CL molecules associated with Aac2. Related to Fig. 2, MSMS performed against Aac2 + 3CL + CATR complex (*m/z* 5069 Da). Increased high collision dissociation (HCD) yielded spectra corresponding to CL (~1400 Da) and CATR (~770 Da).

fig. S3

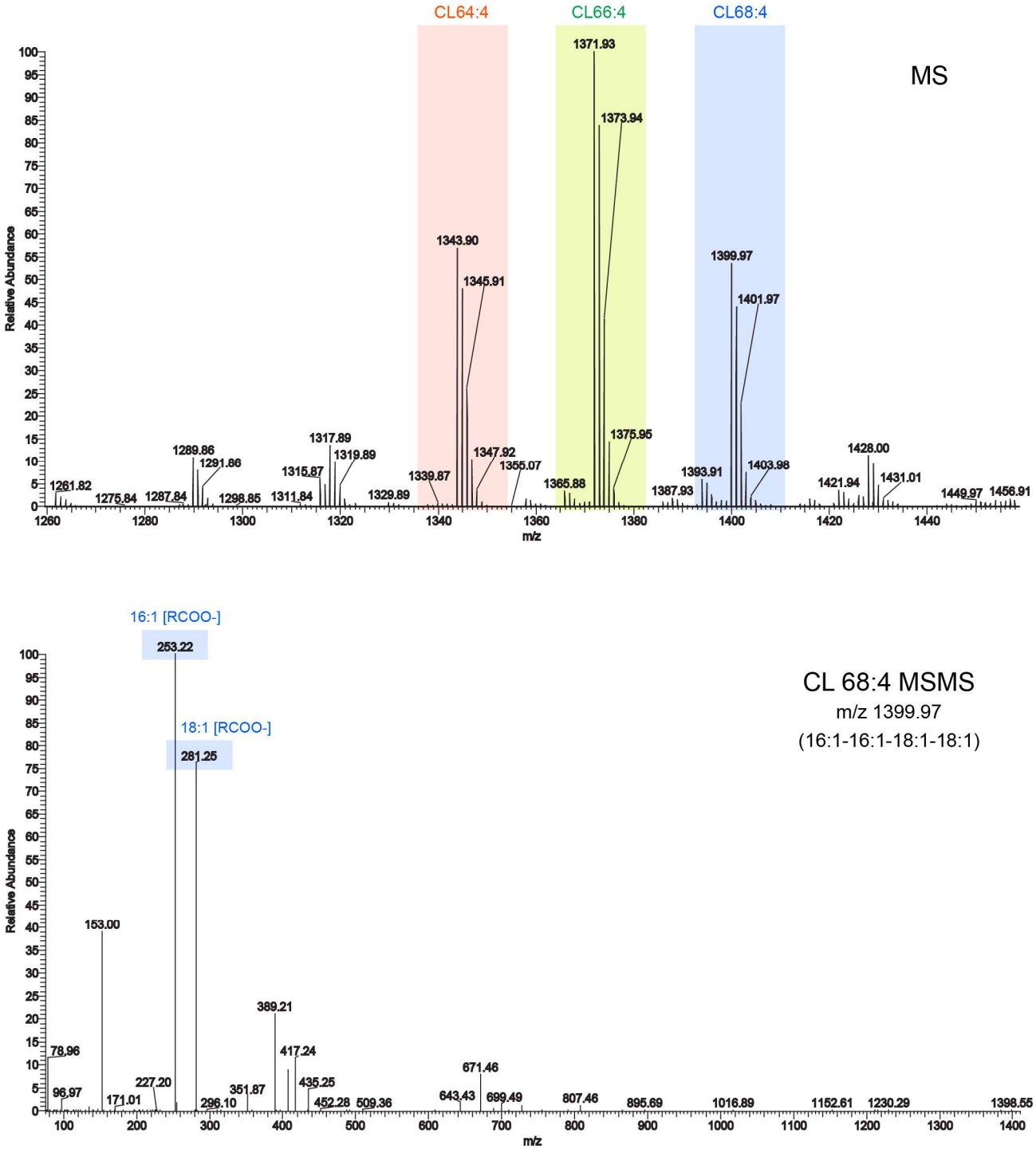

fig. S3: CL species interacting with yeast Aac2. Mass spectrometry (MS) analysis detected three types of CL species that co-purified with FlagAac2 from WT mitochondria (Top). MSMS performed against CL 68:4 yielded unique fragments corresponding to acyl-chains derived from CL (Bottom).

fig. S4

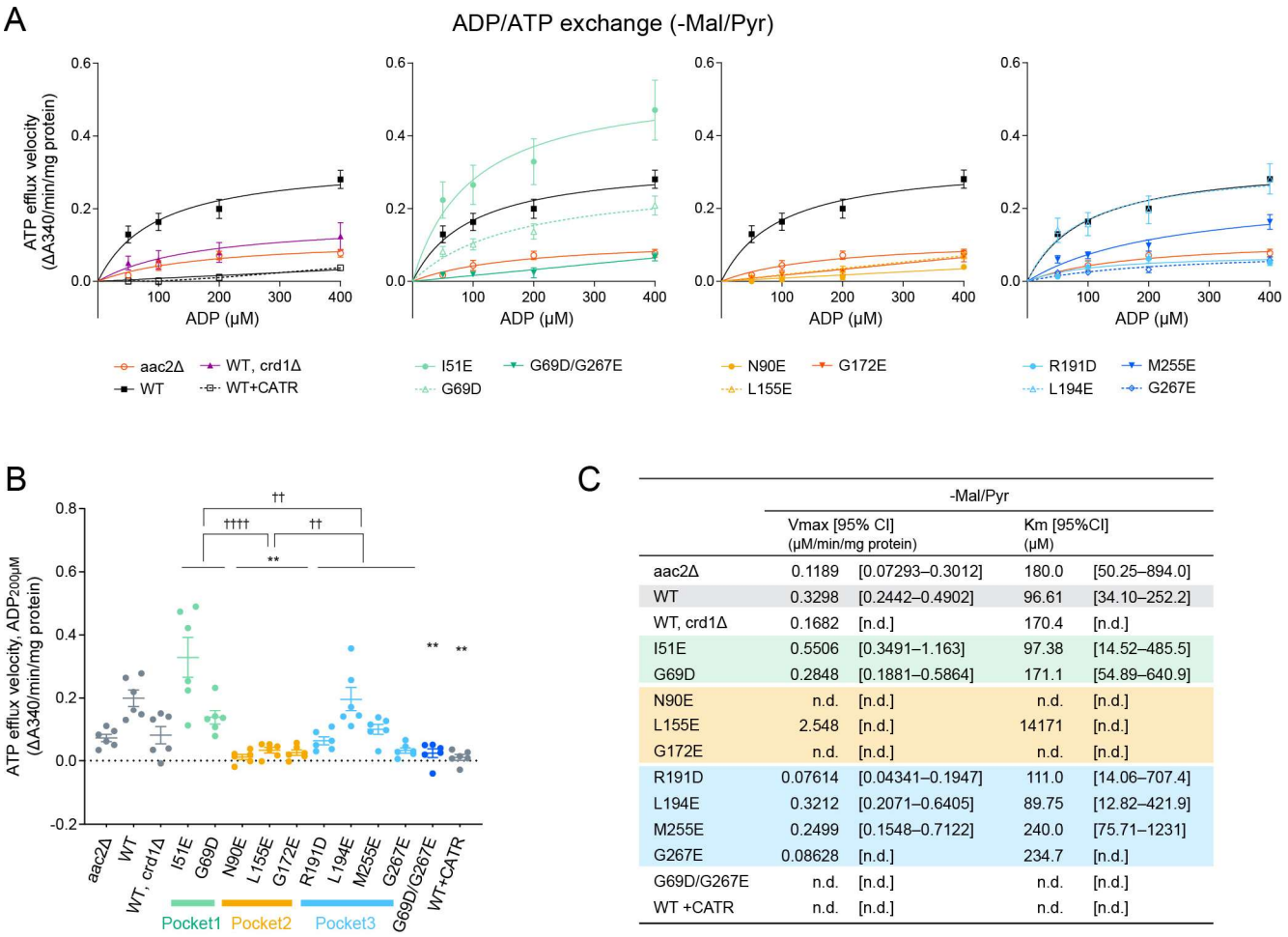

	-Mal/Pyr			
	Vmax [95% CI] (μM/min/mg protein)		Km [95%CI] (μM)	
aac2Δ	0.1189	[0.07293–0.3012]	180.0	[50.25–894.0]
WT	0.3298	[0.2442–0.4902]	96.61	[34.10–252.2]
WT, crd1Δ	0.1682	[n.d.]	170.4	[n.d.]
I51E	0.5506	[0.3491–1.163]	97.38	[14.52–485.5]
G69D	0.2848	[0.1881–0.5864]	171.1	[54.89–640.9]
N90E	n.d.	[n.d.]	n.d.	[n.d.]
L155E	2.548	[n.d.]	14171	[n.d.]
G172E	n.d.	[n.d.]	n.d.	[n.d.]
R191D	0.07614	[0.04341–0.1947]	111.0	[14.06–707.4]
L194E	0.3212	[0.2071–0.6405]	89.75	[12.82–421.9]
M255E	0.2499	[0.1548–0.7122]	240.0	[75.71–1231]
G267E	0.08628	[n.d.]	234.7	[n.d.]
G69D/G267E	n.d.	[n.d.]	n.d.	[n.d.]
WT +CATR	n.d.	[n.d.]	n.d.	[n.d.]

fig. S4: ADP/ATP exchange of Aac2 CL-binding mutants without respiratory substrates. The efflux of matrix ATP was detected with isolated mitochondria as in Fig. 4A-C. The measurement was performed in the absence of malate and pyruvate (-Mal/Pyr). WT + CATR: WT mitochondria were treated with 5 μM CATR prior to the efflux reaction (n=6). (A) The linear part of the initial velocity for the ATP efflux was plotted and curve fitting performed by nonlinear regression (mean with SEM). Plots of *aac*2Δ and WT are repeated in all panels. (B) The initial linear velocity following the addition of 200 μM ADP shown as scatter plots (mean with SEM). (C) Fitted Km and Vmax values were obtained using the Michaelis-Menten equation (mean).

fig. S5

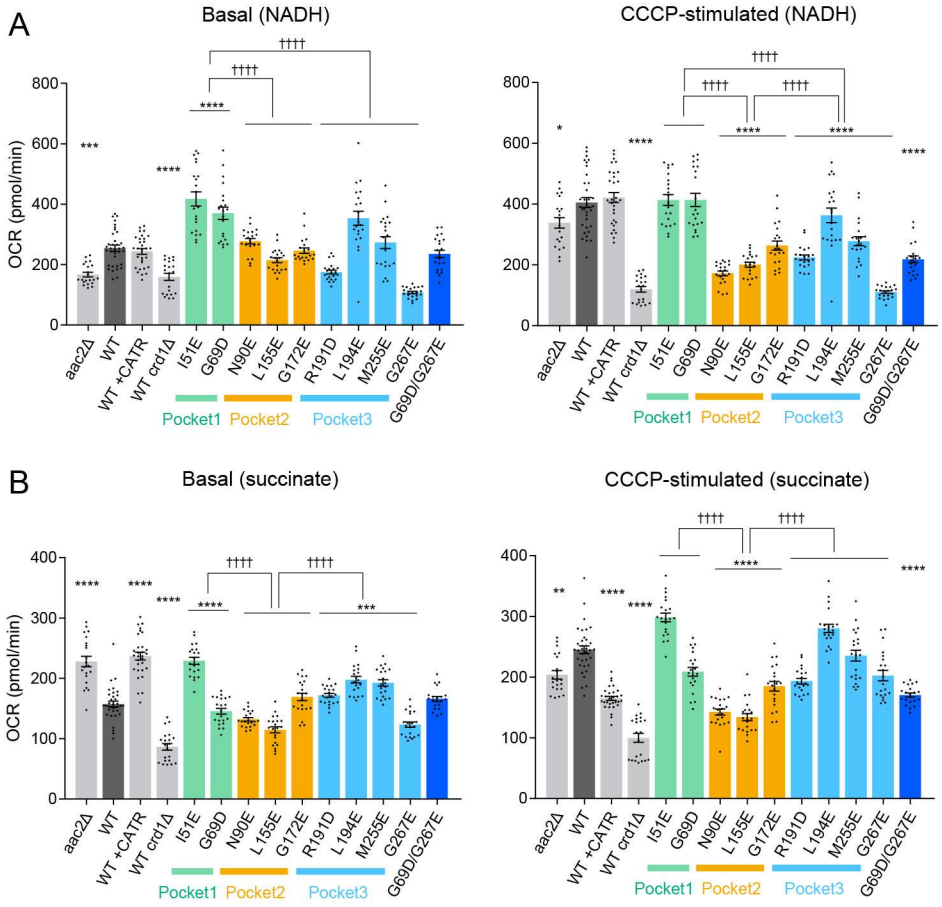

fig. S5: Mitochondrial respiration of Aac2 CL-binding mutants. Related to Fig. 4D-F, basal and CCCP-stimulated respirations of WT and mutant mitochondria in the presence of NADH (A) and succinate (B) were plotted as oxygen consumption rate (OCR). Mean with SEM, n=21-35. Significant differences obtained by two-way ANOVA followed by Tukey's multiple comparisons test are shown as * for comparison with WT and † for comparison between pockets; *p<0.05, **p<0.01, ***p<0.001, ****p<0.0001.

fig. S6

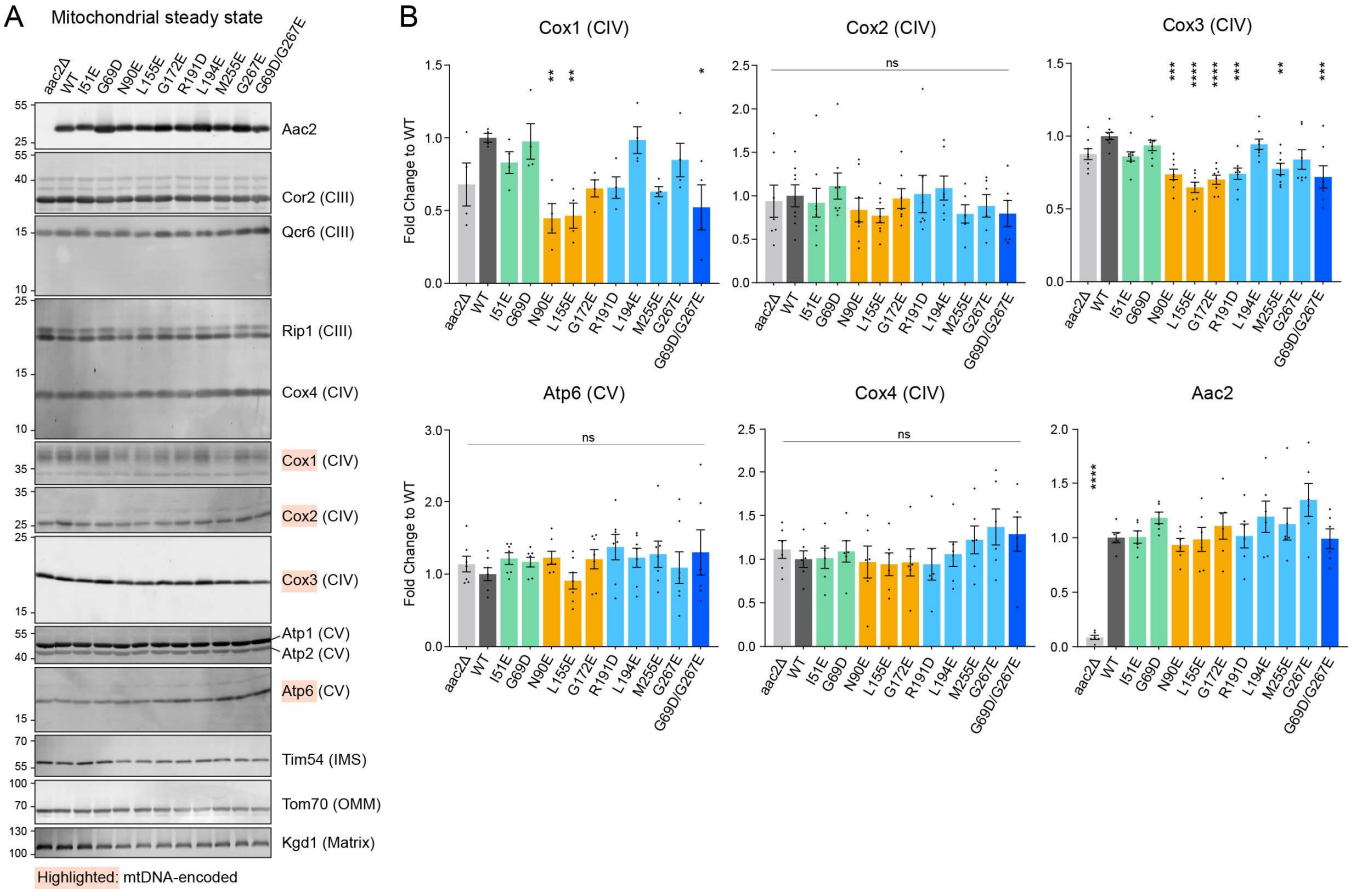

fig. S6: The expression of respiratory complex subunits encoded in mitochondrial DNA is attenuated in Aac2 CL-binding mutants. (A) Mitochondrial extracts were resolved by SDS-PAGE and immunoblotted for indicated proteins, including subunits of respiratory complexes III, IV, and V. (B) The expression of indicated respiratory complex subunits was quantified. Mean with SEM. Statistical differences were analyzed by one-way ANOVA followed by Dunnett's multiple comparison test; *p<0.05, **p<0.01, ***p<0.001, ****p<0.0001 (vs. WT). Representative images from the replicates (n=4-8) are shown.

fig. S7

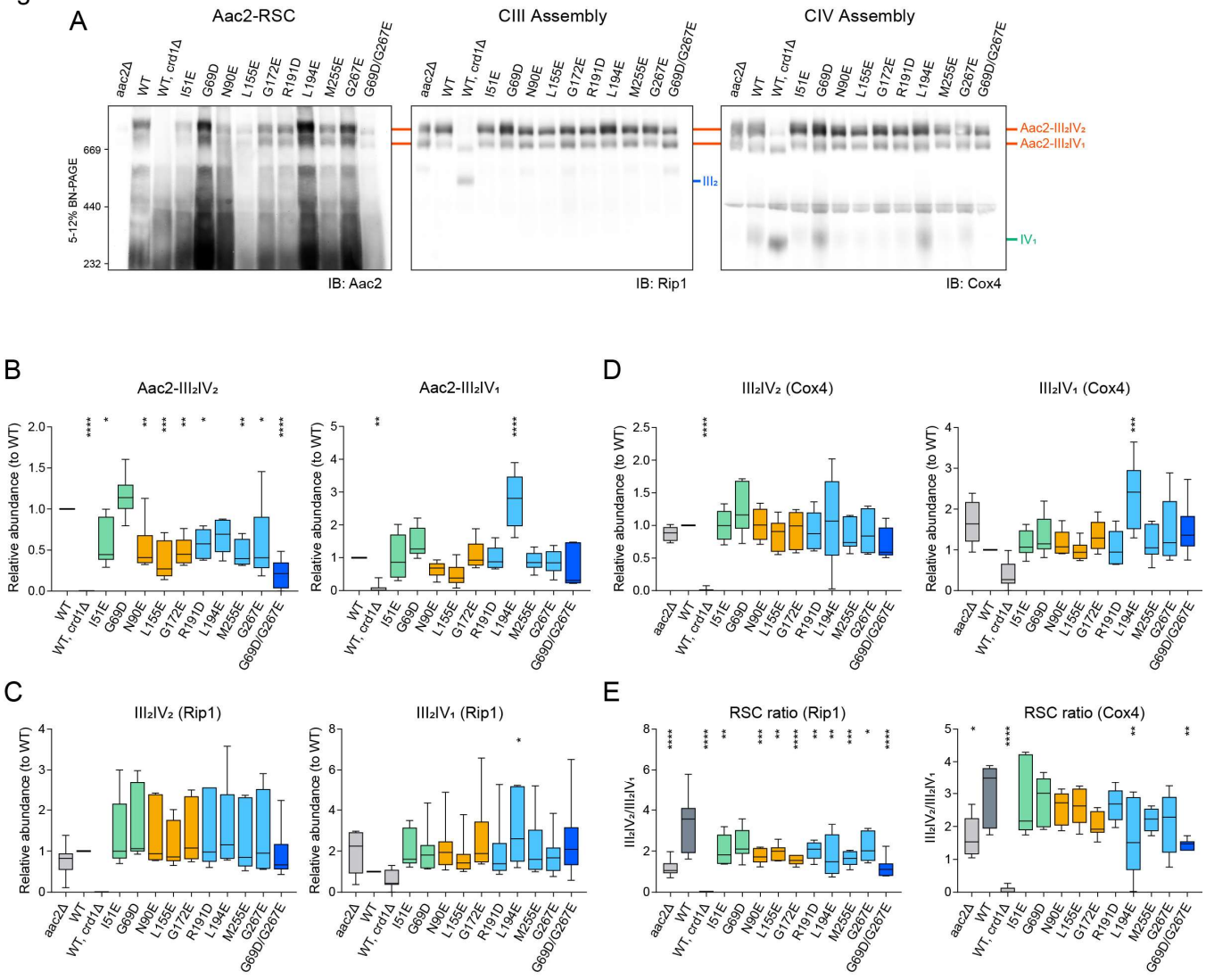

fig. S7: Assembly of Aac2 CL-binding mutants and respiratory supercomplexes is modestly altered. (A) WT and mutant mitochondria were solubilized with 1.5% (w/v) digitonin, resolved by 5 to 12% blue native-PAGE, and immunoblotted (IB) as indicated. RSC, respiratory supercomplex. (B-D) Quantification of assembled Aac2 (B), Rip1 (C), and Cox4 (D) within respiratory supercomplexes. (E) Ratios of respiratory supercomplexes III_2IV_2 and III_2IV_1 when detected by Rip1 and Cox4, respectively. Data are shown as box-whisker plots with the box extended from 25th to 75th percentiles and the whiskers indicating the min to max range. One-way ANOVA followed by Dunnett's multiple comparison test determined the significance; *p<0.05, **p<0.01, ***p<0.001, ****p<0.0001. Representative images from the replicates (n=5-6) are shown; images have been cropped to exclude the abundant Aac2 monomer to facilitate visualization of the Aac2-RSC complexes.

fig. S8

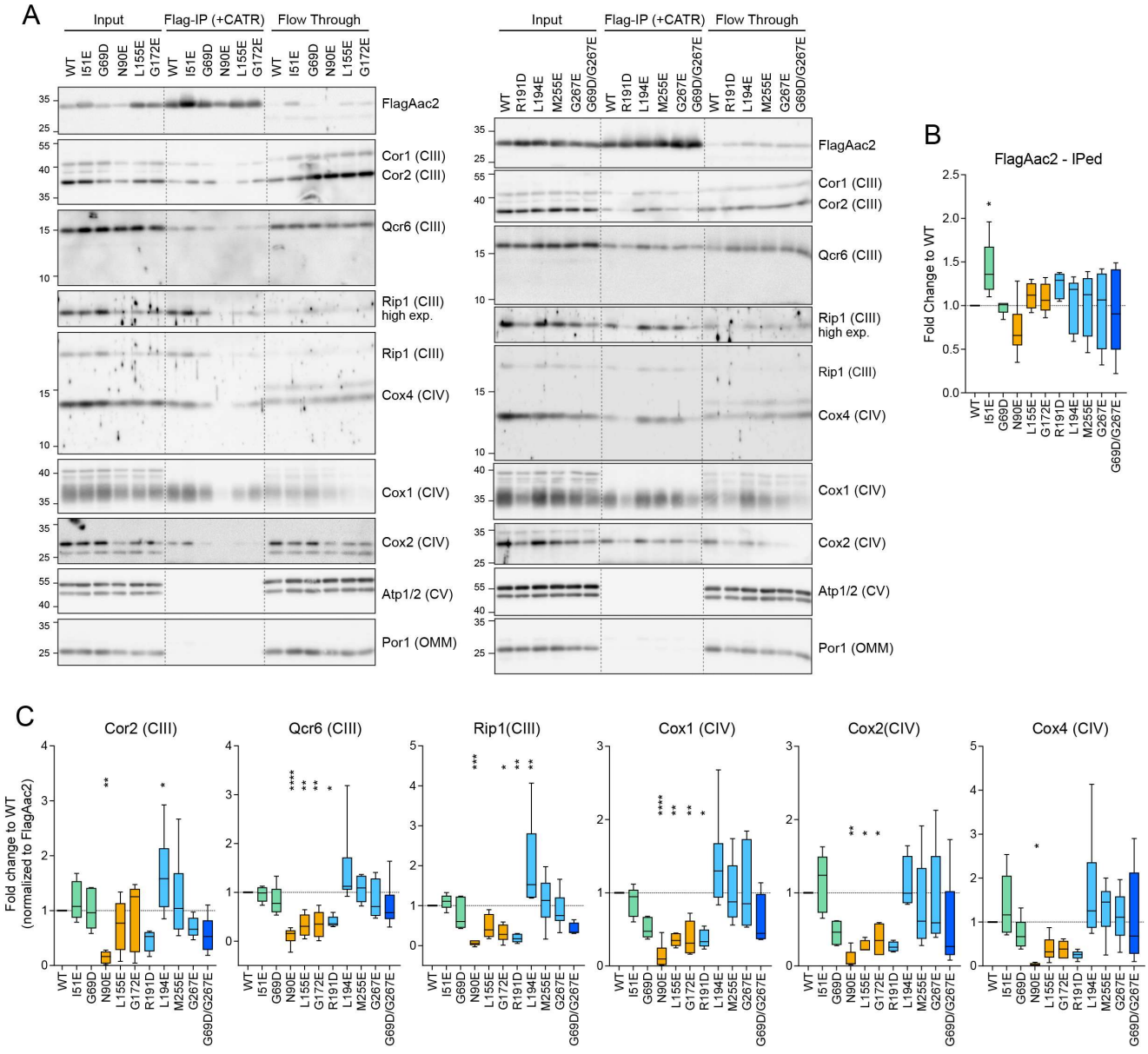

fig. S8: Protein-protein interaction between Aac2 and respiratory complex subunits are diminished in Aac2 CL-binding mutants. (A) Isolated mitochondria from Flag-tagged WT and mutant Aac2 strains were pre-incubated with 40 μM CATR and then solubilized with 1.5% (w/v) digitonin. The mitochondrial extracts were immunoprecipitated (IP) using anti-Flag resin. Co-purified subunits of complexes III and IV were determined by immunoblotting; Atp1/2 and Por1 served as controls. Four percent of input (intact mitochondria) and flow through (unbound) was analyzed. (B) The abundance of FlagAac2 eluted upon IP. (C) The abundance of subunits of complexes III and IV co-purified with FlagAac2 was quantified and normalized. Data are shown as box-whisker plots with the box extended from 25th to 75th percentiles and the whiskers indicating the min to max range. Statistical differences were analyzed by one-way ANOVA followed by Dunnett's multiple comparison test; *p<0.05, **p<0.01, ***p<0.001, ****p<0.0001 (vs. WT). Representative images from the replicates (n=4-12) are shown.

fig. S9

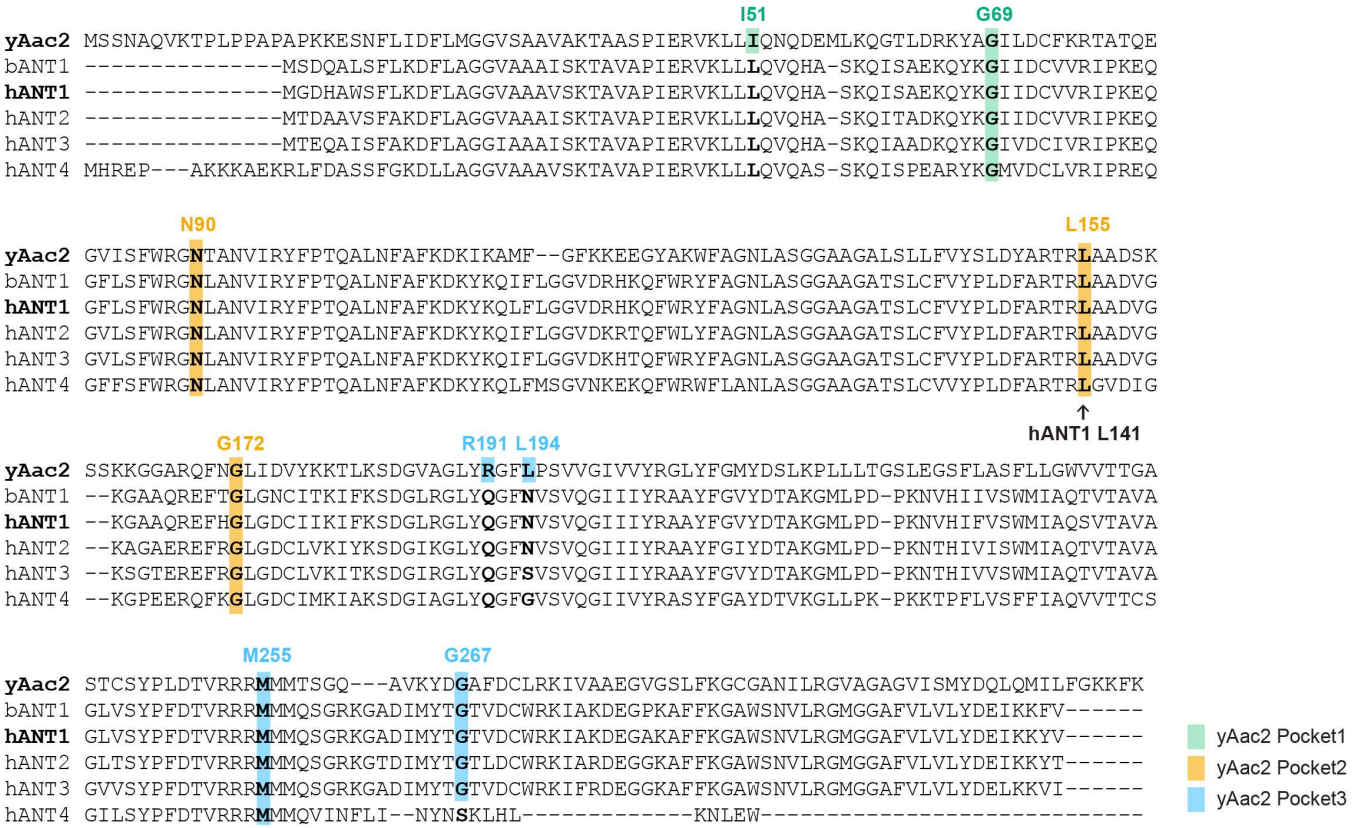

fig. S9: CL-binding sites are conserved across species. Amino acid sequence alignment of yeast Aac2, bovine ANT1, and human ANT isoforms. The residues designed for the Aac2 CL-binding mutants are highlighted as indicated.

fig. S10

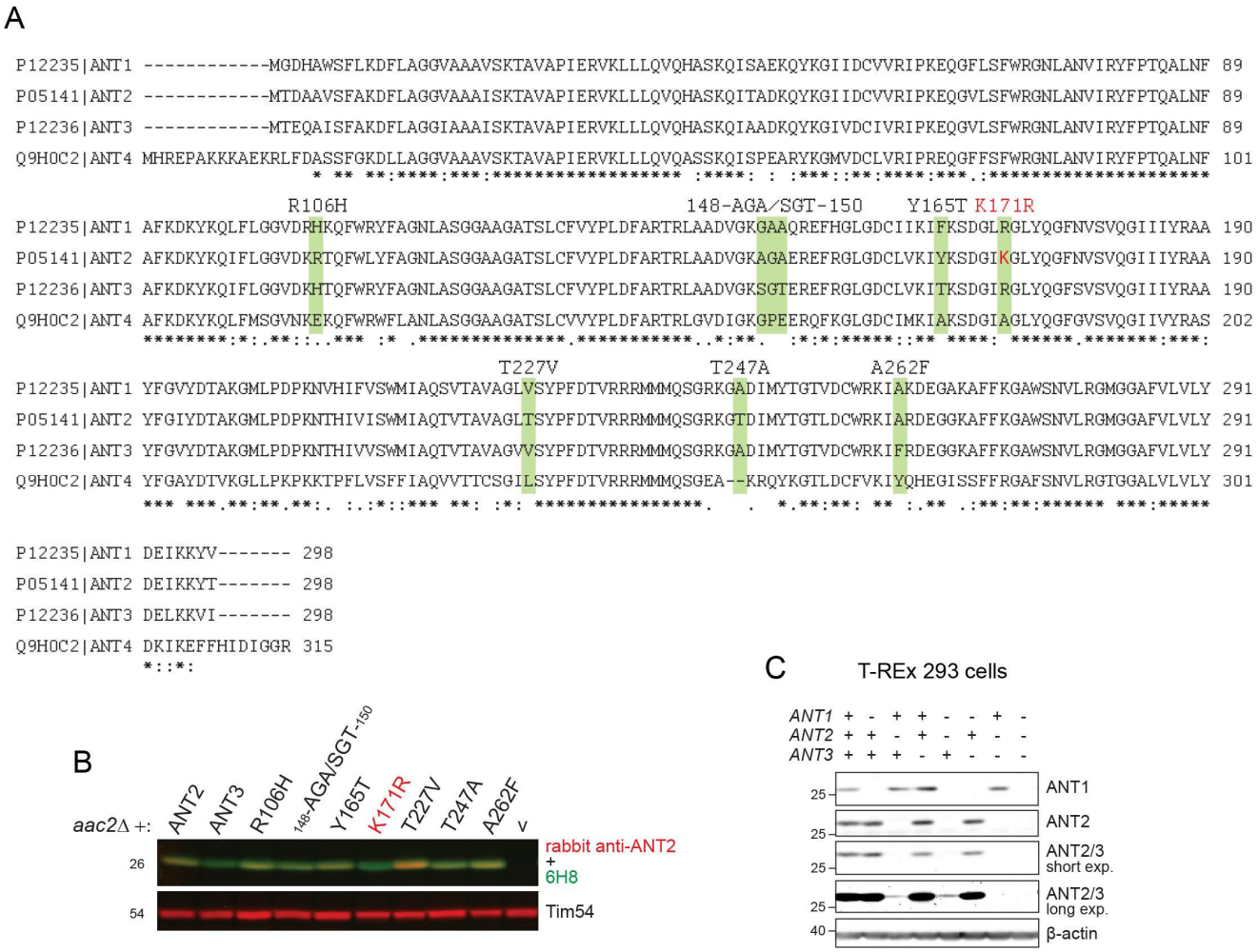

fig. S10: Endogenous expression of three ANT isoforms was absent in ant^{null} cells. (A, B) Peptide mapping of ANT2 antisera. (C) The expression of three ANT isoforms was detected in whole cell extracts by immunoblot (n=5). The absence of ANT1, ANT2, and ANT3 was confirmed in ant^{null} cells (right-most lane). Representative images from the indicated replicates in B and C are shown.

fig. S11

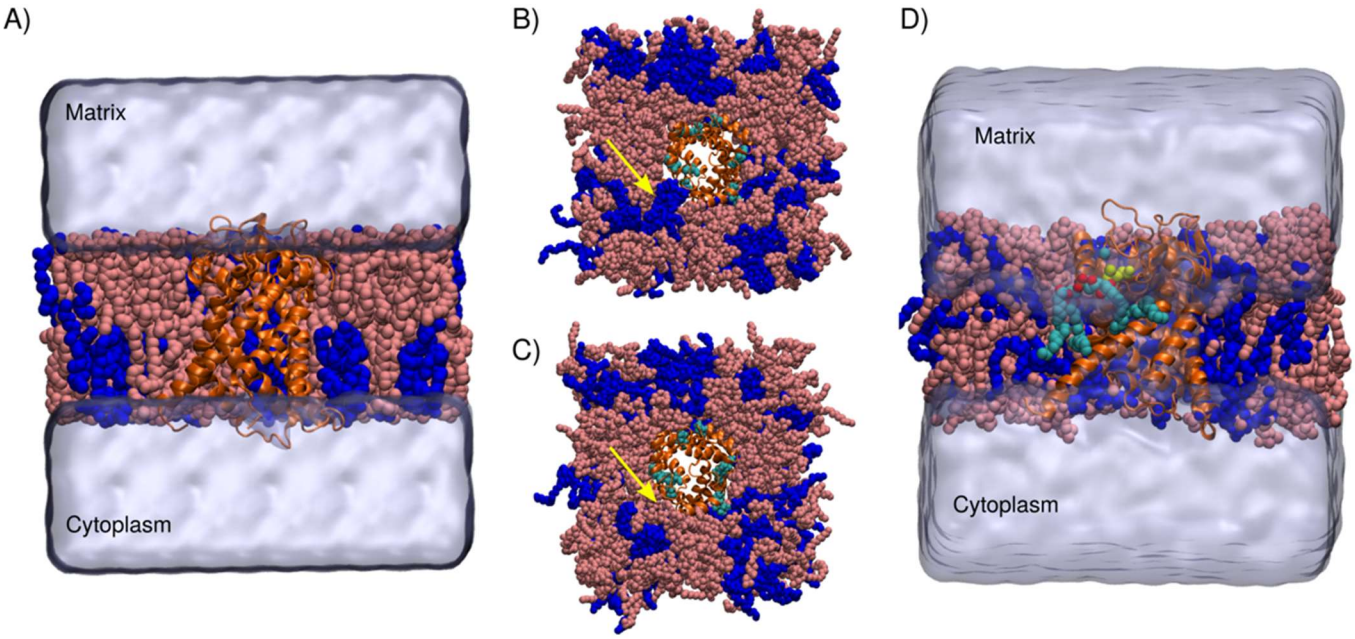

fig. S11: Human ANT1 simulation system setup (c-state). (A) The ANT1 protein (Orange cartoon), POPC (pink), and TLCL2 (tetralinoleoyl-cardiolipin $(18:2)_4$ in di-anionic form) (blue) were solvated in water (iso-blue surface). The top view (matrix view) of the ANT1 system setup for the equilibrium prebound (B) and equilibrium unbound (C) simulations. Yellow arrows point to the presence or absence of CL lipid, around pocket 2. (D) Human ANT1 free energy perturbation (FEP) calculation system setup showing the "ligand CL", LIG (head group oxygen atoms in red, phosphorous atoms in green and acyl chain atoms in cyan van der Waals representation). The front portion of the membrane, hydrogen atoms, and the water molecules were removed for clarity.

fig. S12

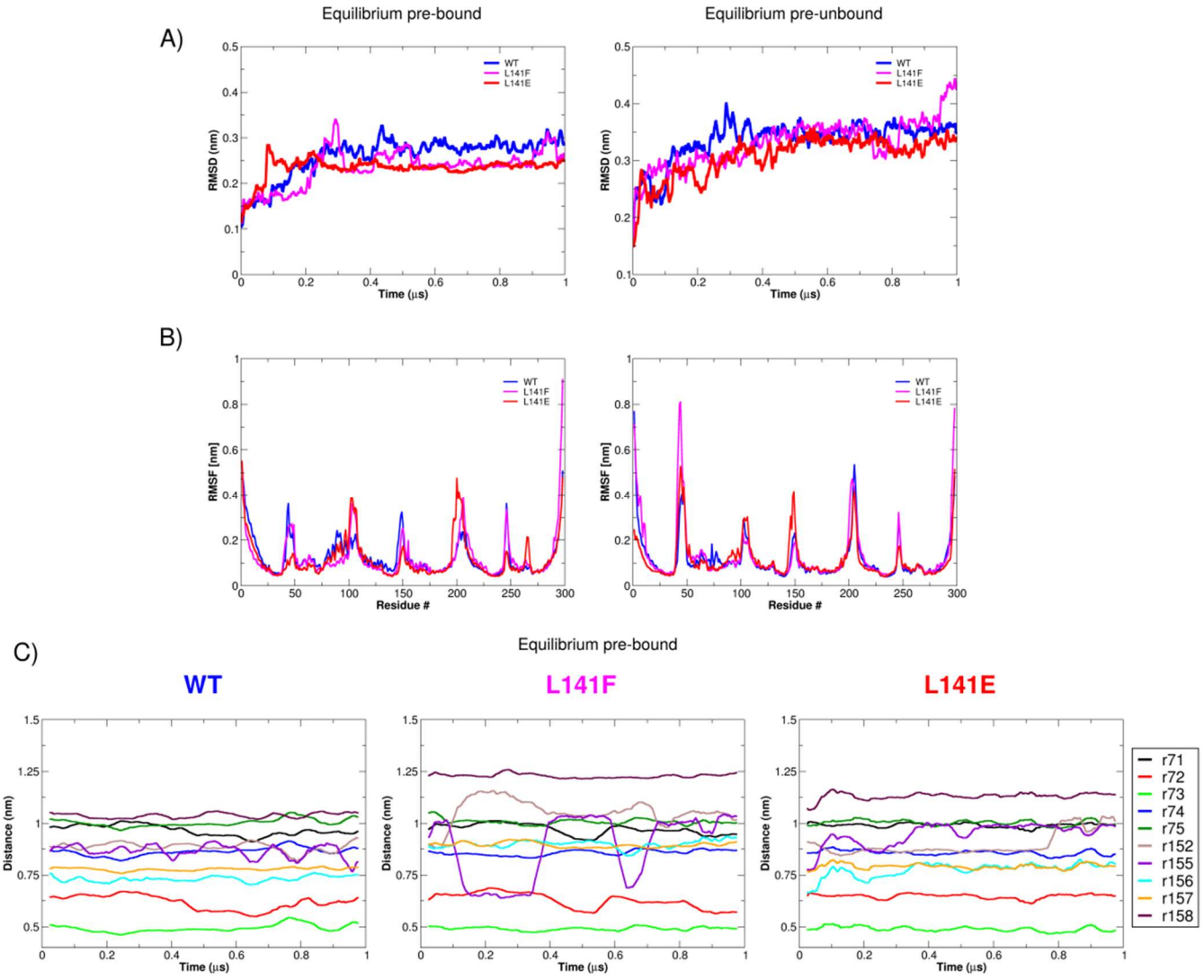

fig. S12: ANT1 protein dynamics during MD simulations. (A) Root-mean-squared deviation (RMSD) in prebound (left) and unbound (right) 1 μs simulations; 100 frame running averaging was performed to smooth the curves. (B) Root-mean-squared fluctuations (RMSF) for prebound (left) and unbound (right) simulations. (C) Calculated distances between the Cα atoms of residue 141 with that of the selected neighboring and pocket 2 binding site residues (residues 71, 72, 73, 74, 75, 152, 155, 156, 157, and 158) during prebound simulations.

fig. S13

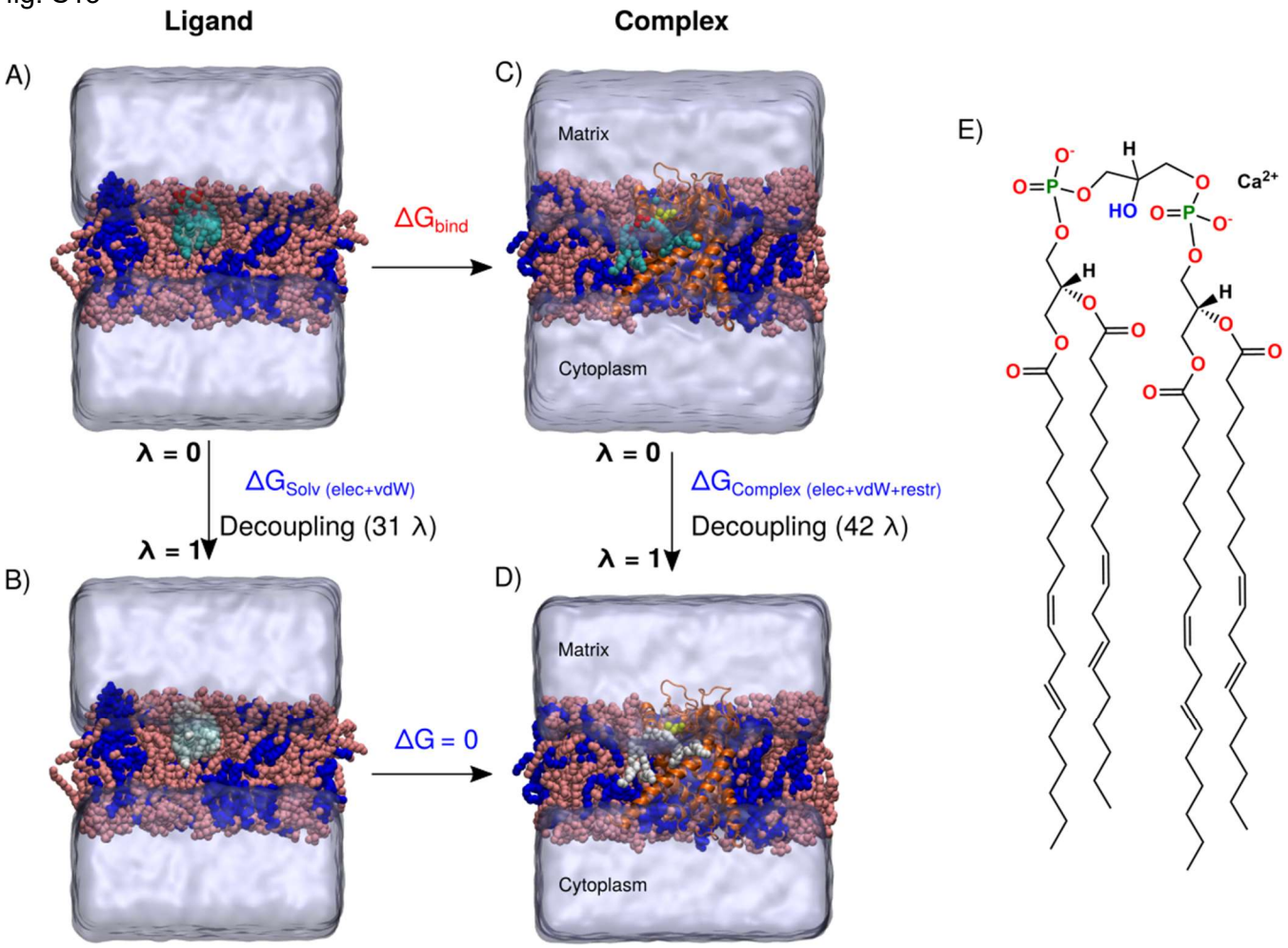

fig. S13: FEP thermodynamic cycle. (A) The fully integrated CL LIG in a bilayer environment is transformed into a completely non-interacting ligand (B, white) during a series of 31 equilibrium simulations in which corresponding electrostatic and van der Waals interactions are scaled to zero. The fully interacting LIG at the top right (C) is transformed into a completely non-interacting ligand (D, white) in the presence of ANT1 membrane protein during a series of 42 equilibrium simulations in which corresponding restraints, electrostatic, and van der Waals interactions are scaled to zero. The ANT1 protein (Orange cartoon), the POPC and TLCL2 membrane lipids (pink and blue van der Waals representation), and ligand LIG (head group oxygen atoms in red, phosphorous atoms in green and acyl chain atoms in cyan van der Waals representation) were solvated in water (iso-blue surface). (E) 2D structure of LIG used in the present study FEP calculations including the Ca^{+2} which was simultaneously decoupled with LIG to maintain charge neutrality.

fig. S14

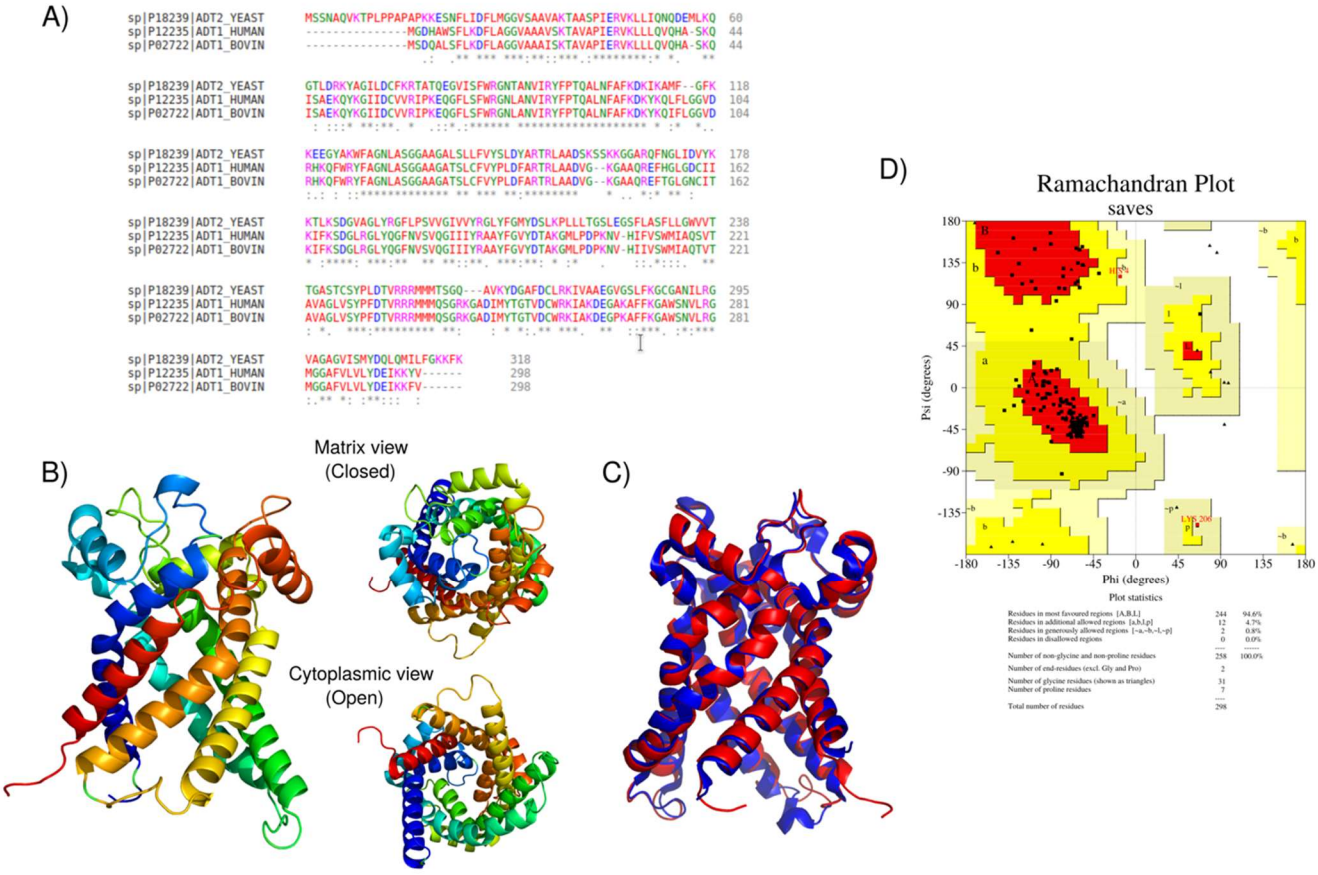

fig. S14: Human ANT1 homology modeling. (A) Sequence alignment of Human ANT1 with Bovine ANT1 and Yeast AAC2. Bovine ANT1 (PDB ID: 1OKC and 2C3E) was used as a template. (B) Cartoon representation of the generated Human ANT1 homology model (97% Quality factor). (C) Overlap structures of Bovine ANT1 (1OKC) and Human ANT1 model proteins. (D) Ramachandran plot of ANT1 model from Human generated by PROCHECK: in which 94.6 % residues in favorable regions; 4.7 % residues in additional allowed regions; 0.8 % residues in generously allowed regions; 0% residues in disallowed regions.

Table S1 Primers used to generate yeast mutant constructs.

Target	Type	Sequence (5'-3')
Aac2 5' UTR (SalI)	Forward	ACGCGTCGACGAGCACTGTTTCCAATGGAG
Aac2 3' End (NotI)	Reverse	GTGGCGGCCGCTCTTATTTGAACTTCTTACCAAAC
Aac2 I51E	Forward	ACTTTTGGAACAAAACCAAGATGAAATGTTAAAAC
Aac2 I51E	Reverse	ATCTTGGTTTTGTTCCAAAAGTTTAACTCTTTCGATGG
Aac2 G69D	Forward	AAAATACGCAGATATCTTAGACTGTTTCAAGAGAAC
Aac2 G69D	Reverse	CAGTCTAAGATATCTGCGTATTTTCTGTCCAAAG
Aac2 N90E	Forward	GGAGAGGTGAGACTGCTAACGTTATCCGTTATTTC
Aac2 N90E	Reverse	GTTAGCAGTCTCACCTCTCCAGAATGAGATAAC
Aac2 L155E	Forward	CAAGAACTAGAGAAGCTGCTGACTCCAAGTC
Aac2 L155E	Reverse	AGCAGCTTCTCTAGTTCTTGCATAATCCAAAG
Aac2 G172E	Forward	GTCAATTCAACGAATTGATCGATGTCTACAAGAAG
Aac2 G172E	Reverse	CGATCAATTCGTTGAATTGACGAGCACC
Aac2 R191D	Forward	GGTCTTTACGACGGTTTCTTACCTTCTGTCGTTG
Aac2 R191D	Reverse	AAGAAACCGTCGTAAAGACCAGCAACACCATC
Aac2 L194E	Forward	CAGAGGTTTCGAACCTTCTGTCGTTGGTATTG
Aac2 L194E	Reverse	CAGAAGGTTCGAAACCTCTGTAAAGACCAG
Aac2 M255E	Forward	AAGAAGAGAGATGATGACCTCCGGTCAAGC
Aac2 M255E	Reverse	GAGGTCATCATCTCTCTTCTTCTAACGGTATCCAATG
Aac2 G267E	Forward	GTTAAGTACGACGAAGCCTTTGACTG
Aac2 G267E	Reverse	AAAGGCTTCGTCGTACTTAACAGC
Aac2 L155F	Forward	AAGAACTAGATTCGCTGCTGACTCCAAGTCCTC
Aac2 L155F	Reverse	GAGTCAGCAGCGAATCTAGTTCTTGCATAATCC

Aac2 N-term Flag	Forward	ATGGATTATAAAGATGATGACGATAAAATGTCTTCCAACGCCCAAGTC
Aac2 N-term Flag	Reverse	TTTATCGTCATCATCTTTATAATCCATGGCTATTTGCTTATATGTATGTTAATGT

Table S2 Primers used to generate human mutant constructs.

Target	Type	Sequence (5'-3')
ANT1 5' Flag (HindIII)	Forward	CCCAAGCTTATGGATTATAAAGATGATGACGATAAAATGGGTGATCACGCTTGGAG
ANT1 3' End (NotI)	Reverse	ATTTGCGGCCGCTTAGACATATTTTTTGATCTC
ANT1 L141E	Forward	GCTAGGACCAGGGAGGCTGCTGATGTGGGCAAG
ANT1 L141E	Reverse	ATCAGCAGCCTCCCTGGTCCTAGCAAAGTCCAGC
ANT1 L141F	Forward	GCTAGGACCAGGTTCGCTGCTGATGTGGGCAAG
ANT1 L141F	Reverse	ATCAGCAGCGAACCTGGTCCTAGCAAAGTCCAGC

Table S3 Antibodies used in this study.

Antibodies	Source	Identifier	Used in
Flag, mouse monoclonal (M2)	Sigma-Aldrich	F3165	fig. S1B
Flag, mouse monoclonal (12C6c)	Developmental Studies Hybridoma Bank (DSHB)	RRID:AB_2890618	Fig. 5C, E; Fig. 6B, C;
Flag, rabbit polyclonal	Sigma-Aldrich	SAB4301135	fig. S8A
Aac2, mouse monoclonal (6H8)	Panneels et al. 2003, Biochem Biophys Res Commun [36]	6H8	Fig. 1B, D; Fig. 3A, B; fig. S7A; fig. S10B
Tom70, rabbit polyclonal	Riezman et al. 1983, EMBO J [87]	7305	Fig. 1B, D, Fig. 5C; fig. S6A
Atp1/2, rabbit polyclonal	Maccecchini et al. 1979, Proc Natl Acad Sci [88]	UY3-T	fig. S6A; fig. S8A
Por1, rabbit polyclonal	Daum et al. 1982, J Biol Chem [89]	425	fig. S8A
Kgd1, rabbit polyclonal	Glick et al. 1992, Cell [90]	453-3	Fig. 1B, Fig. 5C; fig. S6A
Cor2, rabbit polyclonal	Glick et al. 1992, Cell [90]	CC2-T	fig. S6A; fig. S8A
Cox1, rabbit polyclonal	Dowhan et al. 1985, EMBO J [91]	DD2-4	fig. S6A; fig. S8A
Cox2, rabbit polyclonal	Poyton et al. 1975, J Biol Chem [92]	173	fig. S6A; fig. S8A

Cox3, mouse monoclonal (DA5BC4)	Invitrogen	459300	fig. S6A
Cox4, rabbit polyclonal	Baile et al. 2013, Mol Biol Cell [93]	MGB65	fig. S6A; fig. S7A; fig. S8A
Rip1, rabbit polyclonal	Baile et al. 2013, Mol Biol Cell [93]	MGB71	fig. S6A; fig. S7A; fig. S8A
Qcr6, rabbit polyclonal	Baile et al. 2013, Mol Biol Cell [93]	MGB73	fig. S6A; fig. S8A
Atp6, rabbit polyclonal	Kabala et al. 2014, Biochimie [94]	N/A	fig. S6A
Taz, rabbit polyclonal	Claypool et al. 2006, J Cell Biol [59]	4248	Fig. 1D
Abf2, rabbit polyclonal	Calzada et al. 2019, Nat Commun [55]	5477	Fig. 1D
Tim54, rabbit polyclonal	This study	7303	fig. S6A; fig. S10B
β-actin, mouse monoclonal	Sigma-Aldrich	A5441; RRID:AB_476744	Fig. 6B, fig. S10C
GRP75, mouse monoclonal	Antibodies Incorporated	75-127; RRID: AB_2120479	Fig. 6B
ANT1, mouse monoclonal (1F3F11)	Lu et al. 2017, Mol Cell Biol [58]	N/A	fig. S10C
ANT2, rabbit polyclonal	Acoba et al. 2021, Cell Rep [56]	5695	fig. S10B, C
ANT2/3, mouse monoclonal (5H7)	Panneels et al. 2003, Biochem Biophys Res Commun [36]	N/A	fig. S10C
HRP-conjugated secondary, goat anti-rabbit IgG (H+L)	Thermo Fisher Scientific	31460; RRID:AB_228341	Fig. 1B, D; Fig. 3A, B; Fig. 5C, E; Fig. 6 B, C; fig. S1B; fig. S7A; fig. S8A; fig. S10B
HRP-conjugated secondary, goat anti-mouse IgG (H+L)	Thermo Fisher Scientific	62-6520; RRID:AB_2533947	Fig. 1B, D; Fig. 3A, B; Fig. 5C, E; Fig. 6 B, C; fig. S1B; fig. S7A; fig. S8A; fig. S10B
Daylight 650 conjugated secondary, goat anti-rabbit IgG (H+L)	Invitrogen	84546	fig. S6
Daylight 550 conjugated secondary, goat anti-mouse IgG (H+L)	Invitrogen	84540	fig. S6

Table S4 Overview of the simulation setup and details.

Simulation Methods	System	Simulation length
Equilibrium Pocket 2 CL prebound	WT	1 X 1 μs
	L141F	1 X 1 μs
	L141E	1 X 1 μs
Equilibrium Pocket 2 CL unbound	WT	1 X 1 μs
	L141F	1 X 1 μs
	L141E	1 X 1 μs
Free Energy Perturbations (FEP)	WT (42 X 15 ns)	4 X 0.63 μs = 2.52 μs
	L141F (42 X 15 ns)	4 X 0.63 μs = 2.52 μs
	L141E (42 X 15 ns)	4 X 0.63 μs = 2.52 μs
	Ligand (31 X 15 ns)	4 X 0.465 μs = 1.86 μs
		Total = 15.42 μs